

Sinusoidal crossflow microfiltration device—experimental and computational flowfield analysis

Michał M. Mielnik,^{*a} Rahul P. Ekatpure,^{bc} Lars R. Sætran^a and Friedhelm Schönfeld^b

Received 31st January 2005, Accepted 13th May 2005

First published as an Advance Article on the web 10th June 2005

DOI: 10.1039/b501490e

We present an analysis of the flowfield inside a novel crossflow microfiltration device. The filter performance relies on shear focusing by means of a corrugated channel. The flow and shear stress characteristics inside the filter are studied by means of both micro Particle Image Velocimetry (micro-PIV) measurements and Computational Fluid Dynamics (CFD) analysis. We show that an increase of the shear rate by 55–85% as compared to a straight channel geometry is achieved for crossflow velocities ranging from 0.05 m s^{-1} – 0.8 m s^{-1} (Re 5–70). This substantial increase in the local wall shear may improve filter performance in terms of reduced clogging and cell cake formation as compared to conventional crossflow filtration devices. Our current investigation, along with the fact that the filter employs no complex, three dimensional geometrical patterns, advanced pumping schemes, nor has a need for costly assembly and sealing procedures, indicates that the sinusoidal crossflow microfiltration module may serve as a technically and economically feasible solution for integrated lab-on-a-chip devices. Furthermore, the presented approach of shear-focusing may be beneficial in other bio-chemical contexts, such as cell lysis and surface chemistry.

Introduction

The successful development of bio-MEMS devices performing on-chip analysis of biological fluids containing particles like bacteria, viruses, and cells, requires integration of processes such as separation, concentration, mixing, lysis and detection, preferably onboard one single microfluidic chip. Furthermore, each process should allow for continuous operation, as mechanical parts such as valves, plungers and fluidic switches are both complicated and expensive to manufacture.

Crossflow microfiltration is a widely used method for filtration and pre-concentration of macromolecules, colloids, microorganisms and emulsion droplets,¹ and is also applicable for pre-concentration of cells in bio-MEMS devices. The method is based on pumping the suspension of interest through a channel or capillary tube containing one or more porous walls. Due to a pressure gradient across the wall membranes (Trans Membrane Pressure, TMP), the suspending liquid along with particles smaller than the membrane pore size permeates through the walls, while larger particles are retained within the bulk flow inside the channel. The resulting suspension emerging from the microfiltration device accordingly contains a higher concentration of the particles or

biological species of interest. The retentate may then be processed or recycled through the microfiltration channel in order to achieve even higher particle concentration.

This membrane-based filtration method does, however, suffer from diminishing performance under continuous operation conditions in terms of permeate flux reduction and clogging. This is partly due to the growth of a cell (or particle) cake on the channel wall surfaces,² and partly due to internal fouling in terms of deposition and adsorption of particles within the pore structure of the membrane wall.³ Various methods have been pursued and applied in order to improve the performance of crossflow filters, either by pretreatment of the feed fluid itself, by careful choice of material and pore distribution in the membrane, or by manipulation of the flow inside the filtration device. For a given suspension and membrane properties, the enhancement of the shear rate at the liquid/membrane interface is one of the major mechanisms preventing cake formation and fouling of the membrane. In consequence, high crossflow velocities are necessary in order to maintain acceptable permeate fluxes. Various methods for enhanced shear stress generation and breakup of the cake layer have been investigated. Triggering of turbulent flow has been shown to reduce the effects of fouling due to the accompanying increase in wall shear.³ Helically coiled hollow-fiber membranes, promoting the formation of Dean vortices, have been reported to yield an increase of permeate flux by a factor of 2 when applied for filtration of colloidal suspensions.⁴ Secondary flow patterns, induced by screw thread vortex generators inserted in tubular membranes, have been shown to increase fluxes between 50 and 300% as compared to conventional crossflow filters. Various pumping schemes such as backflushing, backshocking, and pulsatile flow exhibit improvements of permeate flux (see *e.g.* Wakeman and

^aNorwegian University of Science and Technology, Dept. of Energy and Process Engineering, Kolbjørn Hejes vei 2, N-7491 Trondheim, Norway. E-mail: michal.mielnik@ntnu.no; Fax: +47 7359 3491; Tel: +47 7359 3714

^bInstitut für Mikrotechnik Mainz GmbH, Dept. of Fluidics, Math. Modelling and Sensors, Carl-Zeiss-Str. 18-20, 55129 Mainz, Germany. E-mail: schoenfeld@imm-mainz.de; Fax: +49 6131 990205; Tel: +49 6131 990 411

^cEindhoven University of Technology, Dept. of Chemical Engineering and Chemistry, P.O. Box 513, 5600 MB Eindhoven, The Netherlands. E-mail: r.p.ekatpure@student.tue.nl

Williams³ and references therein). Microfiltration systems employing mechanical vibration of the membrane, thus creating fields of high shear decoupled from the crossflow velocity, have been reported to yield high permeate fluxes at low crossflow velocities.⁵

The movement of particles in fluid flows is complex and among others depends on their shape, deformability, and density.^{6,7} In the low density limit, neutrally buoyant deformable particles tend to migrate away from the channel walls, whereas rigid spheres experience radial migration only if a sufficiently high Reynolds number is applied.^{6,7} Basically, all industrial crossflow applications rely on large flowrates and correspondingly high shear rates to promote particle migration and to counteract clogging of the filter.

Considering the integration of crossflow microfiltration units in lab-on-a-chip systems, the specific device should preferably be two-dimensional due to fabrication feasibility, and rely on continuous, unidirectional flow to allow for a simple pumping solution. Complex, three-dimensional geometries incorporating advanced pumping schemes such as those described above are thus not the economically and technically preferable approach. For the same reason, the use of different materials such as porous filtration units and a solid support should be omitted, since assembly and sealing on the microscale might be costly.

In this paper, we present an analysis of the flow conditions in a novel crossflow microfiltration module, developed in a collaboration between NorChip AS, Norway and IMM, Germany. The device consists of a sinusoidally shaped microchannel with permeate outlets, or slits, located at the narrowest cross-sections of the channel (hereafter termed *bottlenecks*). We show that the sinusoidal channel shape results in considerable shear focusing at the bottlenecks at moderate (and constant) crossflow velocities as compared to conventional devices.

The functionality of the filters has been tested using aqueous suspensions of latex beads and formaldehyde stabilized leukocytes in pre-treated blood.⁸ Here, we focus on the investigation of the velocity fields. The flow inside the module is studied by means of Computational Fluid Dynamics (CFD) and compared to experimental data acquired by micro Particle Image Velocimetry (micro-PIV) measurements^{9,10} and flow visualization, showing good agreement in the obtained results. The presented data indicate that the sinusoidal crossflow microfiltration module may serve as a feasible solution for integrated lab-on-a-chip devices.

Channel layout and fabrication

The filtration modules (approximately 13 mm × 26 mm) are comprised of parallel rows of sinusoidally shaped microchannels. Two types of filtration modules were manufactured and investigated; one containing 45 small channels, and another containing 24 larger channels. In the following, dimensions for the larger channel structure are given in brackets. A schematic illustration of a single sinusoidal microchannel is shown in Fig. 1. The geometry of the channel was selected based on preliminary CFD calculations. The channel width $2h$ at the bottleneck is 150 μm (300 μm), and 250 μm (500 μm) at the

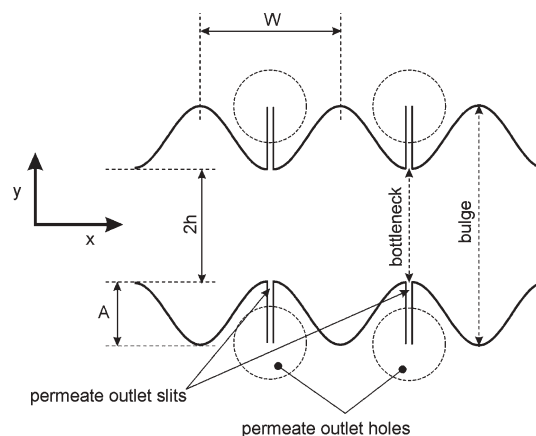


Fig. 1 Schematic illustration of a single sinusoidal microchannel. The dimensions for the small (large) channels are as follows: Bottleneck: $2h = 150 \mu\text{m}$ (300 μm); bulge: $2h = 250 \mu\text{m}$ (500 μm); $W = 105 \mu\text{m}$ (210 μm); $A = 50 \mu\text{m}$ (100 μm). The permeate outlet slits are 5 μm (10 μm) wide. The channel depth is about 50 μm (80 μm).

widest cross-section (hereafter termed *bulge*). The wavelength of the sinusoidal wall is $W = 105 \mu\text{m}$ (210 μm), the amplitude $A = 50 \mu\text{m}$ (100 μm), and the channel depth is about 50 μm (80 μm). The total channel length is 26 mm. The permeate outlet slits are 5 μm (10 μm) wide covering the whole depth of the channel. The permeate outlet holes penetrate the material and emerge at the back side of the filtration module.

Details concerning the fabrication will be presented elsewhere. Briefly, the fabrication of the filtration modules comprised the following processing steps. First, the micro structures, *i.e.* sinusoidal walls and filtration slits, were realized by means of advanced silicon etching (ASE[™]) of the top side of a silicon wafer. Second, permeate outlet holes, inlet and retentate ports were etched from the back side. The top side of the wafer was then covered with Pyrex[™] glass by means of anodic bonding. A single wafer (5") contained four filtration units, which were separated by means of a special wafer saw. Finally, the units were mounted in a polymethyl methacrylate (PMMA) housing containing fluidic connections for the inlet, outlet and permeate outlet flows.

Experimental

Micro-PIV setup

The flowfield inside the sinusoidal crossflow filter was studied experimentally by micro-PIV, employing a standard setup (see *e.g.* Meinhart *et al.*¹⁰). Deionized water (18.2 M Ω cm) seeded with fluorescent polystyrene beads (Molecular Probes) with excitation and emission peaks of 540 nm and 560 nm, respectively, was used as the working fluid for all experiments. The particles have a density of 1005 kg m⁻³ and a diameter of $d_p = 1 \mu\text{m}$. The seeding load was 0.05% (per volume). Triton X-100 (Sigma-Aldrich) was added to the working fluid in order to ensure dispersity of the particle suspension, and to prevent particles from sticking to the channel walls. A syringe pump (PHD 2000 from Harvard Apparatus) was used to drive the working fluid through the microfluidic device. The flow field

was illuminated by a frequency-doubled, double-pulsed Nd:YAG laser (Minilite PIV from Continuum), emitting at a wavelength of 532 nm and thus serving as excitation source for the fluorescent particles. An optical fiber with liquid core and plastic cladding was used to deliver the laser beam to the fluorescence unit of a BX51 microscope from Olympus. The microscope was equipped with appropriate fluorescence filters for imaging of the seed particles and a 20-fold magnification air-immersion objective with numerical aperture (NA) of 0.40. The particle images were recorded by a 10 bit CCD camera (Kodak MEGAPLUS ES1.0/10bit) with an active 1008 by 1018 pixel array and 9 μm pixel-to-pixel spacing, capable of capturing images for cross-correlation with 1 μs time delay between frames. For all experiments, image pairs were captured at a framerate of 8 frames per second (fps). The images were transferred to a PC via a RoadRunner frame-grabber from Bitflow. For further details on the micro-PIV system setup, see Mielnik and Sætran.¹¹

As the seeding concentration was insufficient to perform direct interrogation of individual image pairs while obtaining the desired resolution, an image overlapping procedure was adopted.^{11–13} A total of 80 image pairs were sampled at statistically independent times for each flow velocity. Sets of 16 image pairs were overlapped to form five well-seeded cross-correlation images, and interrogated using an adaptive scheme with final spot size of 32×16 pixels (streamwise \times spanwise direction) and one refinement step (*i.e.* initial interrogation area of 64×32 pixels). Solid boundaries were masked out with zeros prior to interrogation, and all interrogation areas overlapped by the walls by more than 30% were rejected. Finally, the resulting vector fields were averaged. All interrogation was performed using the FlowManager software from Dantec.

Spatial resolution and measurement depth

The interrogation area size (32×16 pixels) translates to a spatial resolution of $14.4 \mu\text{m} \times 7.2 \mu\text{m}$ in the measurement plane in the streamwise and spanwise directions, respectively. The out-of-plane resolution of a micro-PIV system may be estimated by:¹⁴

$$\delta_z = \frac{3n\lambda_0}{NA^2} + \frac{2.16d_p}{\tan \theta} + d_p \quad (1)$$

where δ_z is the measurement depth (or depth of correlation) defined as twice the distance from the focal plane to the position where the particle image intensity is 10% of that of a focused particle. NA is the numerical aperture of the objective lens, d_p is the particle diameter, θ is the half-angle of the light collecting cone of the objective, n is the refractive index of the imaging medium and λ_0 is the wavelength of the illuminating light. For the current experimental setup, δ_z calculated from eqn. (1) was found to be $17.6 \mu\text{m}$. In order to verify this estimate, a series of validation experiments were performed in a square $100 \times 100 \mu\text{m}^2$ cross-section borosilicate glass capillary (Wale Apparatus, Inc.) and compared to the analytical solution for laminar square channel flow. The volumetric flow rate was measured independently of the velocity field and used as input to the analytical solution for

calculation of the velocity distribution over the cross-section of the channel. The micro-PIV measurements were performed in the central horizontal plane of the channel, which was found by focusing the camera on the top and bottom walls, and adjusting the microscope objective to a plane midway between the wall planes. The error in locating the central plane of the flowfield is estimated to be $\pm 3 \mu\text{m}$. This error is mainly due to the focal depth of the optical system and the resolution of the vertical adjustment knob of the microscope stage. The velocity field for three different flowrates was measured. The interrogation procedure was identical to the one applied in the sinusoidal channel experiments as described above.

The measured velocity field was found to underpredict the maximum velocity at centerline by approximately 20% as compared to analytical calculations for the same volumetric flowrate conditions. This discrepancy is of similar magnitude as that found by Park *et al.*¹⁵ for flow in a circular capillary with diameter of $99 \mu\text{m}$, measured with a $40\times$, NA = 0.75 objective. In our case, the underprediction of maximum velocity corresponds to an averaging of the flow velocity over $60 \mu\text{m}$ in the out-of-plane direction, *i.e.* $\pm 30 \mu\text{m}$ relative the central plane of the channel. The velocity profile calculated from the analytical flow solution, achieved by averaging over the above indicated depth, was found to compare well with the one obtained experimentally over the entire span of the channel. The comparison was repeated and confirmed for two additional flow velocities. The experimentally determined measurement depth deviates substantially from the estimate given by eqn. (1). This deviation may possibly be attributed to the fact that eqn. (1) is derived for high-NA objectives (light collecting cone half-angle close to 90° , which is not the case in our setup. The discussion of this matter is, however, beyond the scope of the current investigation, and will not be further addressed here. Nevertheless, the deviation between the calculated and measured value suggests that the depth of correlation of a micro-PIV system should be experimentally determined for each specific optical setup in order to ensure correct values.

In consequence, all experimental data for the larger structure (depth $80 \mu\text{m}$) presented in the following is depth-averaged over $60 \mu\text{m}$, as indicated by the square channel experiments. For the structure containing the smaller sinusoidal channels (depth $50 \mu\text{m}$), the presented micro-PIV data corresponds to full-depth averages of the velocity field. For comparison purposes, all CFD results are averaged accordingly.

Flow visualization

In addition to micro-PIV measurements, qualitative visualizations of the flow field were performed. Deionized water seeded with $1 \mu\text{m}$ diameter fluorescent (560/620) polystyrene particles (Duke Scientific, Inc.) was used as the working fluid. The particle load in the visualizations was 0.01% (per volume). The particles were illuminated by a continuous Hg-arc lamp, and particle streak images were recorded by the CCD camera. The visualizations were performed in the central plane of the sinusoidal channel. The depth of integration of these recordings is expected to be of the same order as that in the micro-PIV experiments.

Flow modelling

The CFD model comprises a single sinusoidal channel (smaller design, dimensions as stated above) with a total length of ten wavelengths. Due to symmetry, only one quarter of the channel geometry was modelled. The simulations were performed on hexahedral grids of typically 3.6×10^5 cells, using the flow solver CFX 5.7 (ANSYS). The channel width and height were resolved with at least 25 cells. In order to assess the accuracy of the derived numerical results, the dependence of local velocities on the grid resolution of the CFD calculations was studied. For this purpose, a Richardson extrapolation for the velocities as a function of $1/(\text{number of grid cells})$ was computed. As a result the numerical error of the values presented below can be safely assumed to be below 0.45%. Furthermore, a rectangular channel having the same cross section as the sinusoidal channel waist (bulge) was simulated. The numerically derived shear rates deviate at most by 1% from the analytical solution (for the series expansion of the flow profile see *e.g.* Hartnett and Kostic¹⁶).

Results and discussion

Zero permeate flow conditions

Permeate flowrates in conventional crossflow devices typically constitute only a fraction of the overall flowrate (10% or less). Thus, in order to analyze the basic flowfield and shear characteristics of the sinusoidal crossflow filter design, an analysis of the flow at zero net permeate flux conditions was performed. These flow conditions were achieved by sealing the permeate outlet slits of the sinusoidal crossflow filter structure by a silicone elastomer membrane. CFD and experimental results for flowfield characteristics and shear rate distribution are presented in the following.

Flowfield characteristics

The velocity field inside the larger sinusoidal channel measured using micro-PIV is shown in Fig. 2a). The figure shows every 3rd column and every 2nd row of vectors. Corresponding

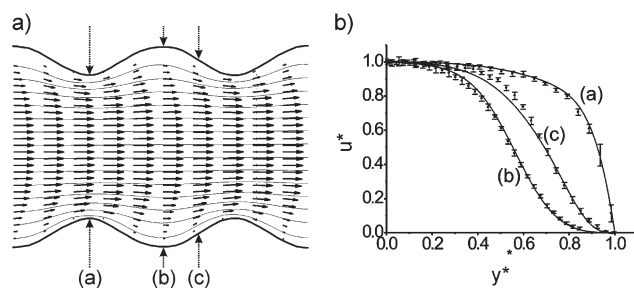


Fig. 2 a) Velocity vector field and corresponding streamlines inside the sinusoidal channel for $Re = 9.4$ and zero net permeate flux conditions (micro-PIV measurements). Every 3rd column and every 2nd row of vectors is shown (large channel geometry). b) Velocity profiles of the sinusoidal channel flow at three different streamwise positions ($Re = 40$): (a) bottleneck; (b) bulge; (c) intermediate position. The symbols represent micro-PIV data, lines denote CFD simulations. y^* is the normalized transversal coordinate, u^* is the normalized streamwise velocity.

streamlines are included in the figure as solid lines. The centerline velocity (depth averaged) is 0.063 m s^{-1} , and the Reynolds number is $Re = 9.4$. The Reynolds number is here defined as $Re = uD_h/\nu$, where u is the centerline velocity, D_h is the average hydraulic diameter (*i.e.* based on channel depth and average width; in this case $80 \mu\text{m} \times 400 \mu\text{m}$) and ν is the kinematic viscosity of water. The velocity field is characterized by accelerated flow in the near-wall regions at the bottlenecks, and slow flow in the bulges of the sinusoidal channel. The streamline patterns indicate that the flow field is unidirectional in the central part of the channel. The influence of the sinusoidal wall shape extends approximately $h/2$ from the side walls into the flow, *i.e.* a distance roughly corresponding to the channel depth.

The velocity profiles at three different streamwise positions (bottleneck, bulge and intermediate position) in the sinusoidal channel are presented in Fig. 2b)). As can be seen from the graphs, an excellent agreement between the micro-PIV measurements and the CFD simulations is obtained. The flow velocity is here normalized by the maximum (depth-averaged) centerline velocity, *i.e.* $u^* = u/u_{\text{max}}$, and the spanwise position relative the centerline is normalized by the local channel half-width at the relevant cross-section, *i.e.* $y^* = y/h$. The Reynolds number is approximately $Re = 40$. The velocity profile at the bottleneck is characterized by a steep velocity gradient at the wall. At the bulge, the profile contains a distinct inflection point appearing at a distance from the wall approximately corresponding to the amplitude of the sinusoidal channel wall. The specific characteristics of the profiles will be discussed in greater detail below, in connection with the treatment of shear stress distribution.

Recirculation zones

As the flow velocity is increased beyond a critical Reynolds number, a qualitative change in the flow pattern is observed in terms of the appearance and development of recirculation zones in the bulges of the sinusoidal microchannel. Visualizations of streamlines in the recirculation zones for increasing Re are shown in Fig. 3. The qualitative features exhibited by the computationally and experimentally obtained flowfield images are seen to be nearly identical. For $Re \leq 40$, the flow follows the meandering shape of the walls and no

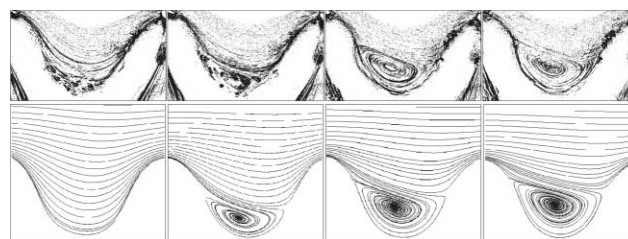


Fig. 3 Development of the recirculation zones in the crossflow microfiltration module with increasing Reynolds numbers (flow from left to right). From left to right: $Re = 20$, no recirculation present; $Re = 42$, commencing recirculation; $Re = 63$, $Re = 85$, distinct recirculation zones. Top: experimental flow visualizations (colours are inverted and grey-scale levels altered to aid visibility). Bottom: CFD simulations. (Large channel geometry.)

separation is observed. As Re increases beyond $Re \approx 40$, separation is observed downstream of the bottlenecks and a small recirculation zone initiates, extending over a limited part of the bulge. For exceeding Re , the recirculation zones expand, finally covering most of the area between the bottlenecks.

From the perspective of filtration purposes, the recirculation zones represent areas of relatively low shear, and may thus potentially function as traps for the cellular material contained within the feed liquid. This, in turn, may result in extensive cell cake formation and growth until finally filling the entire bulges, thus removing the shear-focusing effect initially created by the sinusoidal shape of the channel. Cake formation within the bulge region would, however, also contribute to a reduction of the region itself, thus counteracting the formation of recirculation zones, as their maintenance requires increasing Reynolds numbers as the extent of the bulge diminishes. Furthermore, as can be observed from the streamline visualizations in Fig. 3, mass transfer between the bulk fluid and the recirculation zones is clearly limited, and restricted mostly to the fluid passing directly above the bottleneck wall. Indeed, during flow visualization experiments, it was observed that tracer particles, once captured inside the recirculation zones, did not easily escape. On the other hand, new particles did seldom entrain the recirculation zone from the outer flow once the recirculation was fully established. This highly restricted extent of mass transfer between the outer flow and the recirculation zones may attenuate formation of a cell cake in the bulge regions even at the low shear rates experienced in these areas.

Shear stress distribution

The filtration performance depends to a large extent on the wall shear stress at the bottlenecks, *i.e.* at the locations of the permeate outlet slits. Fig. 4 shows the shear rate at the bottlenecks as a function of the local Reynolds number (defined by the local average velocity and cross-section dimensions), presenting data obtained from both CFD simulations and micro-PIV measurements. The shear rate is seen to increase monotonically with increasing Re . The agreement between the micro-PIV and CFD data is generally good, with discrepancies in accordance with the experimental uncertainty for the near-wall velocity data presented in Fig. 2b). Note that the evaluation of the derivatives amplifies the uncertainties connected to experimental (and numerical) data acquisition.

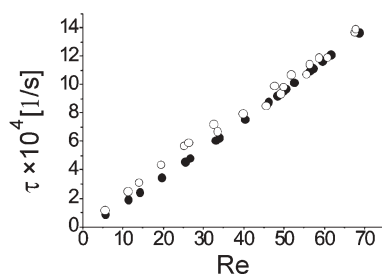


Fig. 4 Wall shear stress at bottleneck as a function of Reynolds number. Comparison of experimental data (open symbols) and CFD results (solid symbols).

To investigate the shear stress enhancement in detail, we revisit the velocity profiles for the sinusoidal channel flow. CFD results for axial flow velocities as a function of the normalized transversal coordinate, y^* , are shown in Fig. 5. Velocity profiles for flow in corresponding straight rectangular channels with the same flowrate and cross-section are shown for comparison. As can be seen in the figure, the velocity profiles for the sinusoidal channel, specifically the shear rates, are qualitatively different at the bottleneck and the bulge. While in the former case an increased shear rate compared to the rectangular channel is observed, the opposite is true at the bulge. This can be most easily understood in the low Re limit considering the steady state Stokes equation:

$$Re \nabla p = \nabla^2 \vec{u} \quad (2)$$

Compared to the rectangular channel with a uniaxial flow field, the wall shear rate ($\partial u / \partial y$) is modified by the integral over $-\partial^2 u_x / \partial x^2$ in the sinusoidal case. Since the variation of the axial velocity is directly interlinked with the channel cross-section, one finds $\partial^2 u_x / \partial x^2 < 0$ (> 0) at the bottleneck (bulge). Thus, the shear rate is increased and reduced at the narrow and wide cross-sections, respectively. This observation stimulated the basic design idea behind the filter, namely to “focus” the shear rate at the permeate outlets, *i.e.* the filtration slits at the bottlenecks. A further shear focusing is expected to arise for larger Re , *i.e.* if inertial forces come into play. In order to highlight a corresponding non-linear dependence of the shear rate on Re , we normalize it by the shear rate found in a straight channel flow. Indeed, the data ($\tau^* = \tau_{\text{sin}} / \tau_{\text{rec}}$) plotted in Fig. 6 show a nonlinear increase. As can be read off from the figure, a shear rate enhancement of about 55% is achieved in the low Re limit. For higher Re the velocity at the center region is gradually enhanced at the cost of the outer (bulge) flow velocity. For Re above about 40 flow separation sets in. The recirculation zones (*cf.* Fig. 3) lead to a further increase of the wall shear rate, which finally levels off at an increase of approximately 85% for stable, fully developed recirculation zones. As is to be expected, the linear dependence of τ_{sin} on Re , *i.e.* a constant τ^* , commences when the recirculation zones have grown to full size, *i.e.* when they occupy the entire bulge region between the bottlenecks, as any additional increase of

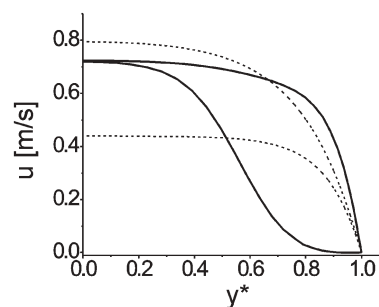


Fig. 5 Velocity profiles of a rectangular and sinusoidal channel in the non-recirculating regime. The upper (lower) solid curve denotes the profile of the bottleneck (bulge) of the sinusoidal channel. The dashed curves show the corresponding velocities of a straight rectangular channel having the same cross-section. y^* denotes the normalized transversal coordinate (small channel geometry).

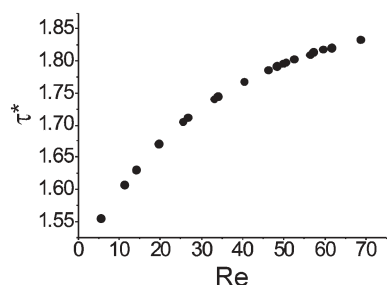


Fig. 6 Shear rate at bottleneck normalized by shear rate in a rectangular channel of the same depth and width as bottleneck, as a function of Reynolds number (CFD data).

the flowrate does not further alter the qualitative features of the flow.

The intermediate and high Re cases inducing transient behavior such as vortex oscillations, vortex-hopping and finally turbulence are beyond the scope of the present article. The substantial increase in the local wall shear contributes to reduction of clogging and cell cake formation in the vicinity of the permeate slits, thus improving filter performance in terms of attenuated permeate flux reduction as compared to conventional filters.

Flow with permeate flux

In order to assess the influence of open permeate slits on shear focusing at channel bottlenecks, a series of experiments in the larger channel geometry filters were performed with varying ratios of permeate-to-total volume flowrates, $Q^* = Q_p/Q_{tot}$. The shear rate τ at the bottlenecks as a function of Re_{bulk} (Reynolds number based on total flowrate and average hydraulic diameter) for four different values of Q^* is shown in Fig. 7. In addition, the case for zero net permeate flux ($Q^* = 0$) is included for comparison. As can be expected, the growth of the shear rate with increasing Re_{bulk} is seen to diminish with increasing values of the permeate flux. Such a trend, however, would also be true for any conventional,

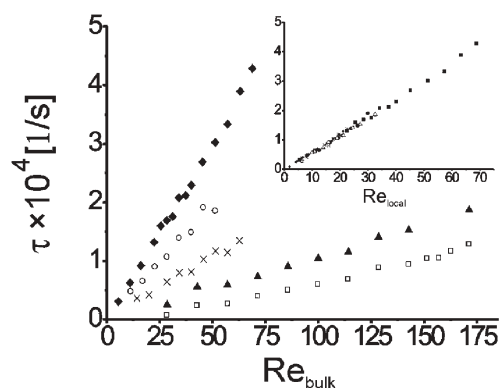


Fig. 7 Shear rate at channel bottleneck as a function of Reynolds number for different ratios of Q^* (micro-PIV measurements). Symbols: $Q^* = \square$ 0.9; \blacktriangle 0.75; \times 0.5; \circ 0.2; \blacklozenge 0 (zero net permeate flow). Re_{bulk} is based on bulk velocity (total flowrate). Inset: Re_{local} is based on the local velocity inside the sinusoidal channel, *i.e.* the retentate flow velocity. All data are taken for the larger channel geometry.

straight crossflow filter. Replotting the data with Re based on the retentate velocity, *i.e.* the local velocity inside the main sinusoidal channel (Re_{local}), results in the graph presented in the inset of Fig. 7. The shear rate data for all four permeate flow cases are seen to collapse onto a single line, coinciding in an excellent manner with the data obtained for zero net permeate flux. This is the case even though the permeate flux-to-overall flowrate ratios analyzed here are excessive as compared to those typically encountered in conventional crossflow filtration devices. This clearly indicates that the local velocity field inside the sinusoidal channel is not significantly altered by the presence of permeate flow, which in turn justifies the general validity of the analysis of the filter at zero net permeate flux conditions presented above.

Summary

A novel crossflow microfilter relying on shear focusing by means of a corrugated channel has been presented. Since, as in conventional crossflow filtration, typical permeate flowrates constitute only a fraction of the overall flowrate, the focus has been put on the flow field analysis for closed permeate outlet slits. The validity of this approach has been verified experimentally. The functionality of the filtration method taking aqueous latex bead suspension and formaldehyde stabilized leukocytes as examples has been proven and will be presented elsewhere.⁸

The flowfield inside the sinusoidal channel was studied by means of CFD simulations and micro-PIV measurements for Reynolds numbers in the range between $Re = 5$ and $Re = 70$. The flow is characterized by high wall shear stress at bottlenecks and low shear stress in the bulges of the channel, which can be understood by considering the low Re limit of the Navier–Stokes equations at steady state. As the Reynolds number increases beyond $Re \approx 40$, recirculation zones develop in the bulges and grow with increasing flowrate. These recirculation zones lead to a further increase in the shear rate. For fully developed recirculation zones ($Re > 70$), a linear relation between shear stress and Re is recovered. At the bottlenecks, the sinusoidal design was found to yield an increase of the shear stress by a factor of 1.55–1.85 as compared to corresponding straight rectangular channel flow. This substantial increase in the local wall shear will contribute to reduction of clogging and cell cake formation in the vicinity of the permeate slits, thus improving filter performance in terms of enhanced permeate flux as compared to conventional devices. The channel structures and the presented flow field analysis should, however, also be considered in other contexts beyond filtration. Shear focusing may, for example, be utilized for mechanical cell lysis, or more generally, it may be applied to enhance mass transfer from/to channel walls.

The presented data indicate that the sinusoidal channel arrays may serve as a feasible solution for integrated lab-on-a-chip devices.

Acknowledgements

The authors gratefully acknowledge cooperation and financial support from NorChip AS, Norway and are indebted to

Lothar Schmitt and Richard Huber (formerly at IMM) for their manufacturing skills. F. Schönfeld acknowledges Steffen Hardt for fruitful discussions and support by the DFG-Forschergruppe FOR 516/1, German Ministry of Research and Education, grant number 16SV1355. M. Mielnik gratefully acknowledges The Research Council of Norway for their financial support of this work (NFR project no. 147028).

References

- 1 S. Ripperger and J. Altmann, *Sep. Purif. Technol.*, 2002, **26**, 19–31.
- 2 K. A. Caridis and T. D. Papathanasiou, *Bioprocess Eng.*, 1997, **16**, 199–208.
- 3 R. J. Wakeman and C. J. Williams, *Sep. Purif. Technol.*, 2002, **26**, 3–18.
- 4 P. Moulin, P. Manno, J. C. Rouch, C. Serra, M. J. Clifton and P. Aptel, *J. Membr. Sci.*, 1999, **156**, 109–130.
- 5 J. Postelthwaite, S. R. Lamping, G. C. Leach, M. F. Hurwitz and G. J. Lye, *J. Membr. Sci.*, 2004, **228**, 89–101.
- 6 R. G. Cox and S. G. Mason, *Annu. Rev. Fluid Mech.*, 1971, **3**, 291–316.
- 7 R. G. Cox and S. K. Hsu, *Int. J. Multiphase Flow*, 1977, **3**, 201–222.
- 8 F. V. Germar and F. Schönfeld, *Institut für Mikrotechnik Mainz GmbH (IMM)*, Germany, personal communication.
- 9 J. G. Santiago, S. T. Wereley, C. D. Meinhart, D. J. Beebe and R. J. Adrian, *Exp. Fluids*, 1998, **25**, 316–319.
- 10 C. D. Meinhart, S. T. Wereley and J. G. Santiago, *Exp. Fluids*, 1999, **27**, 414–419.
- 11 M. M. Mielnik and L. R. Sætran, *Proc. 1st Int. Conf. Microchannels Minichannels*, April 24–25 2003, Rochester, NY, USA, ed. S. G. Kandlikar, ASME, 2003, pp. 887–894, ISBN No. 0-7918-3667-3.
- 12 S. T. Wereley, L. Gui and C. D. Meinhart, *AIAA J.*, 2002, **40**, 1047–1055.
- 13 M. M. Mielnik and L. R. Sætran, *Turbulence*, 2004, **10**, 83–90.
- 14 C. D. Meinhart, S. T. Wereley and M. H. B. Gray, *Meas. Sci. Technol.*, 2000, **11**, 809–814.
- 15 S. J. Park, C. K. Choi and K. D. Kim, *Exp. Fluids*, 2004, **37**, 105–119.
- 16 J. P. Hartnett and M. Kostic, *Adv. Heat Transfer*, 1989, **19**, 247–356.